Correlation between Local Stress and Strain and Lamina Cribrosa Connective Tissue Volume Fraction in Normal Monkey Eyes

Michael D. Roberts,[1] *Yi Liang,*[1] *Ian A. Sigal,*[1] *Jonathan Grimm,*[2] *Juan Reynaud,*[2] *Anthony Bellezza,*[3] *Claude F. Burgoyne,*[2] *and J. Crawford Downs*[1]

Purpose. To investigate the biomechanical response to IOP elevation of normal monkey eyes using eye-specific, three-dimensional (3-D) finite element (FE) models of the ONH that incorporate lamina cribrosa (LC) microarchitectural information.

Methods. A serial sectioning and episcopic imaging technique was used to reconstruct the ONH and peripapillary sclera of four pairs of eyes fixed at 10 mm Hg. FE models were generated with local LC material properties representing the connective tissue volume fraction (CTVF) and predominant LC beam orientation and used to simulate an increase in IOP from 10 to 45 mm Hg. An LC material stiffness constant was varied to assess its influence on biomechanical response.

Results. Strains and stresses within contralateral eyes were remarkably similar in both magnitude and distribution. Strain correlated inversely, and nonlinearly, with CTVF (median, $r^2 = 0.73$), with tensile strains largest in the temporal region. Stress correlated linearly with CTVF (median $r^2 = 0.63$), with the central and superior regions bearing the highest stresses. Net average LC displacement was either posterior or anterior, depending on whether the laminar material properties were compliant or stiff.

Conclusions. The results show that contralateral eyes exhibit similar mechanical behavior and suggest that local mechanical stress and strain within the LC are correlate highly with local laminar CTVF. These simulations emphasize the importance of developing both high-resolution imaging of the LC microarchitecture and next-generation, deep-scanning OCT techniques to clarify the relationships between IOP-related LC displacement and CTVF-related stress and strain in the LC. Such imaging may predict sites of IOP-related damage in glaucoma. (*Invest Ophthalmol Vis Sci.* 2010;51:295–307) DOI:10.1167/iovs.09-4016

From the [1]Ocular Biomechanics and [2]Optic Nerve Head Research Laboratories of the Devers Eye Institute, Legacy Health System, Portland, Oregon; and [3]Third Eye Diagnostics, Inc., Bethlehem, Pennsylvania.

Supported in part by U.S. Public Health service Grant R01EY011610 (CFB) from the National Eye Institute, National Institutes of Health, Bethesda, Maryland; and the Legacy Good Samaritan Foundation, Portland, OR.

Submitted for publication May 20, 2009; revised July 9 and 30, 2009; accepted July 31, 2009.

Disclosure: **M.D. Roberts**, None; **Y. Liang**, None; **I.A. Sigal**, None; **J. Grimm**, None; **J. Reynaud**, None; **A. Bellezza**, None; **C.F. Burgoyne**, None; **J.C. Downs**, None

Corresponding author: J. Crawford Downs, Ocular Biomechanics Laboratory, Devers Eye Institute, 1225 NE 2nd Avenue, Portland OR 97232; cdowns@deverseye.org.

Glaucoma is a progressive degenerative optic neuropathy that is projected to affect nearly 60 million people worldwide by 2010.[1] Although there are numerous factors involved in the pathogenesis of the disease, including vascular dysfunction and ischemia[2,3] and interactions between retinal ganglion cells and the lateral geniculate nucleus and visual cortex,[4] intraocular pressure (IOP) clearly plays an important role at all levels of IOP. IOP reduction remains the only clinically proven approach to slowing or halting disease progression.[5–8]

From a mechanical perspective, IOP exerts a uniform load on the inner eye wall that gives rise to deformations, stresses, and strains within the constituent tissues of the eye. In the posterior pole, the connective tissues of the sclera and lamina cribrosa (LC) play the most important role in bearing IOP-related loads. The connective tissue structures comprising the LC are of particular interest because they span a discontinuity in the scleral shell at the scleral canal and, as such, are located within a region of a substantial IOP-related stress concentration.[9,10] There is ample evidence that the LC is the initial site of insult in glaucoma and its complex connective tissue microarchitecture has been correlated with patterns of vision loss and hypothesized to play a key role in axonal damage.[11] Thus, it has been suggested that the biomechanical environment of the LC and peripapillary sclera plays an important role in the development and progression of glaucoma, either due to direct mechanical effects or via mechanically mediated effects on blood flow, axoplasmic transport, or cellular activation.[10,12]

Although a large body of literature has emerged regarding measurement of the compliance behavior of the surface of the optic nerve head (ONH) during elevated IOP,[13–19] surface position has been shown to be a poor indicator of underlying laminar and peripapillary scleral position (Agoumi Y, et al. *IOVS* 2009;50:ARVO E-Abstract 4898).[19–21] Several researchers have therefore turned to computational models as a method of describing the biomechanics of these connective tissues. Such computational models of the ONH and peripapillary sclera provide predictions of IOP-related deformation, as well as IOP-related stress and strain that are not obtainable by imaging alone.

Bellezza et al.[9] used an idealized model of the posterior pole with a rudimentary LC structure to show that the stresses in the ONH could be substantial, even at normal levels of IOP. Sigal et al. have presented both generic parameterized[19,22] and eye-specific[20,23–25] finite element (FE) models incorporating pre- and retrolaminar neural tissues with scleral, laminar, and pial connective tissues. These parametric studies highlighted the importance of scleral and laminar material properties and scleral thickness on the mechanical environment of the ONH, but suggested that specific details of the ONH geometry had a smaller effect on stresses and strains than expected. Furthermore, Sigal's work demonstrated that IOP-related displace-

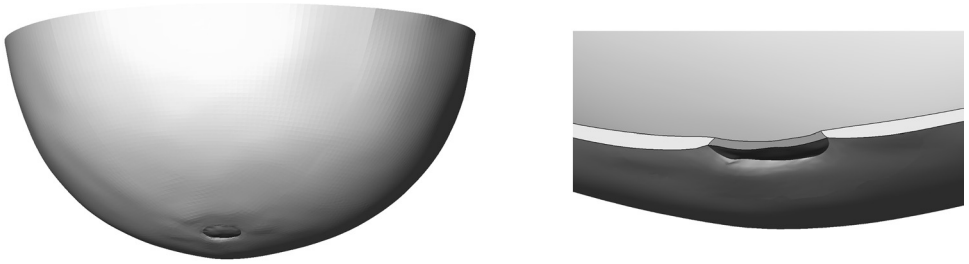

FIGURE 1. Detail of the posterior pole geometry showing the incorporation of the eye-specific LC and peripapillary sclera into a generic scleral shell with anatomic thickness variation.

ments of the ONH surface may not mirror the underlying laminar displacements and that attempts to infer LC deformation from prelaminar neural tissue measurements can be suspect. More recent work has shown that the interactions between geometric and material factors can be just as important as the impact of each factor individually, suggesting that susceptibility to IOP-related damage may depend on the combinations of anatomic and material characteristics that a given eye possesses.[26]

None of these previous modeling studies, however, have accounted for the regional variation in LC microarchitecture, but instead have treated the LC as a homogeneous, isotropic material. In a previous report, we described a method of characterizing the inhomogeneous connective tissue microarchitecture in the LC of the monkey eye.[27] It is likely that the individual-specific microarchitecture of the LC connective tissue (its spatial distribution and orientation) affect the manner in which load is borne throughout the ONH and hence determine its IOP-related deformation. Separate from its microarchitecture, the material properties of the laminar tissues should also play an important role in the mechanical behavior of the LC.

In this study, we incorporated eye-specific LC microarchitectural information into continuum FE models of the LC of paired eyes from four bilaterally normal monkeys that had been perfusion fixed with both eyes at an IOP of 10 mm Hg. We then varied the material properties assigned to this laminar microarchitecture and measured the effect on predicted laminar displacement, neural canal expansion, and laminar strain and stress resulting from a simulated acute IOP elevation from 10 to 45 mm Hg. Our study was designed to address three questions. First, if all other variables are kept constant, to what degree do laminar material properties effect laminar deformation, laminar strain, and laminar stress? Second, to what degree does the biological variation between the two eyes of a normal animal affect these phenomena? Third, are there underlying relationships between laminar microarchitecture and regions of maximum laminar strain and stress that could serve as imaging targets for clinical assessment of glaucomatous susceptibility in the future?

MATERIALS AND METHODS

Animals

Four bilaterally normal rhesus monkeys—three females 8 to 10 years of age, and one male 2 years of age—were used in the present work. Details of the ONH anatomy and LC microarchitecture of these animals have been presented in two previous reports.[27,28] All animals were treated in accordance with the ARVO Statement for the Use of Animals in Ophthalmic and Vision Research.

Three-Dimensional Reconstruction of the ONH and Peripapillary Sclera

The computer models of the LC and peripapillary sclera used in this study were derived from the three-dimensionally reconstructed ONHs from four bilaterally normal rhesus monkeys presented in previous publications.[27,28] Briefly, a microtome-based serial sectioning technique was used to episcopically image an embedded specimen block face to which a connective tissue stain (1:1 volumetric mixture of Ponceau S and acid fuchsin) had been applied after each section cut. High-resolution images were consecutively acquired at 1.5-μm section intervals, stacked, and aligned to produce volumetric histologic datasets (voxel resolution of $1.5 \times 1.5 \times 1.5$ μm) suitable for visualization and morphometric analysis. Tissue boundaries corresponding to the neural canal wall and the anterior and posterior surfaces of the LC and peripapillary sclera were manually delineated in three dimensional (3-D) space by viewing digital sagittal sections through the datasets at 40 consecutive radial cutting planes centered on the ONH and spaced 4.5° apart. The tissue boundaries were then interpolated to form the bounding surfaces of a closed LC region within which a custom volumetric segmentation algorithm was used to classify voxels as either connective or nonconnective tissue.[29] This procedure is discussed in greater detail in Roberts et al.[27]

Incorporation of an Eye-Specific 3-D ONH Reconstruction into the Generic Scleral Shell

The user-delineated 3-D surfaces defining the boundaries of the LC and surrounding peripapillary sclera were incorporated into a generic scleral shell of variable anatomic thickness representing the posterior pole. The scleral shell surface geometry was derived from a digitization of the surface of a representative normal monkey scleral shell acquired using a tactile probe-based scanning system (Picza PIX-4; Roland DGA, Irvine, CA). The eye-specific 3-D ONH reconstructions were incorporated into the generic scleral shell structure by performing a least-squares fit of each eye's anterior scleral canal opening into the continuous anterior scleral shell surface, to set the scleral canal's position.

To obtain anatomic scleral thickness in the model geometries, scleral thickness data from previous studies[30,31] were mapped onto the entire generic posterior scleral shell surface geometry and interpolated to provide a continuous map of scleral shell thickness. Eye-specific peripapillary sclera thickness data from each 3-D ONH reconstruction was calculated from the user-delineated anterior and posterior peripapillary scleral surfaces, as previously described,[32] and then overlaid onto the generic thickness map. The integrated scleral thickness map was determined by considering the zone of overlap ($\sim$1500 μm around the scleral canal) between the generic scleral thickness map and the eye-specific peripapillary scleral thickness map. To maintain continuity between the 3-D-reconstructed LC/peripapillary sclera volume of each eye and the generic posterior pole, the generic scleral thickness map was uniformly scaled to minimize the discontinuity between the eye-specific and generic scleral thickness maps. The scaling value was calculated as the ratio of peripapillary scleral thickness from the eye-specific reconstruction to that from the generic thicknesses in their areas of overlap. The integrated scleral thickness data were then extruded normal to the surface of the digitized shell, to produce a 3-D representation of the scleral shell with continuously variable anatomic thickness. An example of the incorporation of an eye-specific ONH and peripapillary sclera into the generic scleral shell is shown in Figure 1.

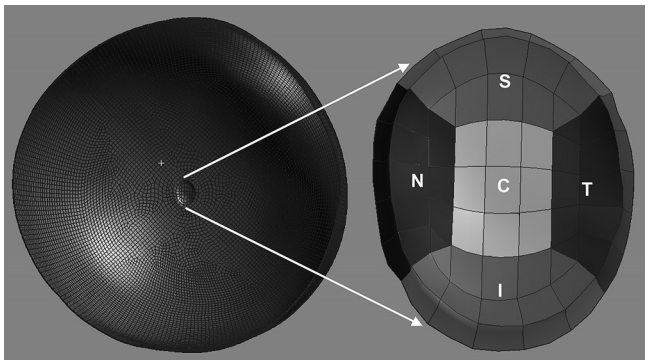

FIGURE 2. Finite element mesh of the posterior pole with a detail of the elements of the LC and the regionalization scheme used for analysis. S, superior; N, nasal; I, inferior; T, temporal; C, central.

FE Model Construction

The FE models in this work consisted of only the LC and scleral tissue of the posterior pole, which are the principal load-bearing connective tissues in that region (Fig. 2). We did not model the prelaminar neural tissues, the pia mater, or the retrolaminar optic nerve. The LC/scleral shell geometry (Fig. 1) was meshed with 20-noded quadratic hexahedral elements with a commercial FE pre- and postprocessing package (PATRAN; MSC Software, Santa Ana, CA). The nodes along the equator of the sclera were constrained to allow movement in the radial direction only. A pressure load of 35 mm Hg was applied to the interior surface of the model to simulate an IOP increase from 10 to 45 mm Hg (the eyes modeled in this study were perfusion fixed at an IOP of 10 mm Hg, and therefore that IOP was considered to be the baseline state). Analyses were performed in a scripted manner with a commercial FE analysis code (ABAQUS ver. 6.1, Hibbitt, Karlsson & Sorensen, Inc., Providence, RI) that calculated the Cauchy true stress and logarithmic strain using large deformation theory (NLGEOM flag in ABAQUS).

Scleral material properties were defined as linear and isotropic and derived from the equilibrium modulus found in uniaxial stress relaxation tests of normal monkey eyes (4.94 MPa).[33,34] For each of the models, we scaled this material property value upward by the same factor used to scale the thickness maps downward during incorporation of the 3-D reconstruction into the generic scleral shell (the scaling factor ranged from 1.7 to 2.5 for all eyes). The rationale for this scaling procedure was that it served to restore structural stiffness (the product of the elastic modulus of the tissue and its thickness[35]) that was lost when scaling the generic scleral thickness map to conform to the eye-specific peripapillary sclera geometry. It should be noted that, for our purposes, the scleral shell in each FE model simply serves to transmit IOP-induced deformation of the scleral canal to the LC, and the scleral canal expansion in these models agrees well with that measured experimentally between bilaterally normal monkey eyes perfusion fixed at IOPs of 10 and 45 mm Hg, respectively.[21]

In a previous report, we described a method for characterizing regional variations in laminar connective tissue microarchitecture.[27] This methodology was leveraged in the present report to assign regional material properties to the LC that reflect the underlying regional volume fraction and predominant orientation of the laminar trabeculae. Briefly, subvolumes of the LC connective tissue were characterized in terms of (1) the local connective tissue volume fraction (CTVF), the relative amount of connective tissue in a sampled volume of tissue within the LC; and (2) the fabric, the predominant LC connective tissue beam orientation in the sampled volume, and the strength of directional anisotropy as quantified by the fabric tensor. These descriptors of the LC microstructure are readily measured in our 3-D reconstructions, reflect eye-specific variation in LC connective tissue distribution and organization, and can be used to calculate the regional directional stiffness of the LC. The fabric, in particular, may be mathematically represented as a 3-D ellipsoid oriented in space whose three mutually orthogonal radii (the eigenvalues of the fabric tensor) represent the relative strength of beam orientation in their respective directions.

In this work, we translated these quantitative descriptions of local laminar microarchitecture into a continuum-level mathematical description of the local directional stiffness of the LC. That is, the details of the microarchitecture were homogenized within FE-sized volumes such that the bulk material properties assigned to each LC element described the local direction-dependent stiffness of the associated enclosed laminar microarchitecture. Specifically, we assumed that the LC could be described as linearly elastic and orthotropic such that the stiffness in three mutually perpendicular directions could assume different values, mimicking an approach used for modeling the microstructure of trabecular bone.[36] These three material stiffnesses and their associated Poisson's ratios and shear moduli were calculated using the following relationships:

$$E_i = A\rho^2 H_i^3 \quad i = 1, 2, 3 \tag{1}$$

$$\nu_{13} = 0.45, \quad \nu_{12} = 0.45\left(\frac{E_2}{E_1}\right), \quad \nu_{23} = 0.45\left(\frac{E_3}{E_2}\right) \tag{2}$$

$$G_{12} = \frac{E_1}{2(1-\nu_{12})}, \quad G_{13} = \frac{E_1}{2(1-\nu_{13})}, \quad G_{23} = \frac{E_2}{2(1-\nu_{23})} \tag{3}$$

where E_i is the orthotropic Young's moduli (MPa); A is a global laminar material constant reflecting the intrinsic stiffness of the LC connective tissue (MPa); ρ is the local connective tissue volume fraction; H_i is the eigenvalues of the local fabric tensor, which reflect the relative degree of orthotropic anisotropy (and therefore directional stiffness) due to the microarchitectural arrangement of the laminar beams; ν_{ij} is the orthotropic Poisson's ratios; and G_{ij} is the orthotropic shear moduli (MPa), where $i, j, = 1, 2, 3$ represents each of the three principal orthotropic material directions unique to each element. We used the convention that the eigenvalues of the fabric tensor were normalized so that $H_1 + H_2 + H_3 = 1$ and were ordered as $H_1 \geq H_2 \geq H_3$, as described in our previous study.[27] Note that the exponent applied to the ρ term in equation 1 is relatively common in porous materials, but that in practice an appropriate value is determined experimentally.[37–41] Similarly, the exponent associated with the eigenvalue terms H_i would typically be determined experimentally. By ordering and normalizing the eigenvalues as described, the effect was to make the $i = 1$ direction—the predominant beam direction— correspond to the greatest stiffness and the two and three directions correspond to the lesser and least stiff directions, respectively.[39,42,43] Finally, the assumed Poisson's ratio of $\nu_{13} = 0.45$ imparts near incompressibility to the tissue in the principal direction and the prescribed value is similar to those reported by Battaglioli and Kamm[44] for bovine sclera.

FE Analyses and Output Measures of Mechanical Response

Because the sampling scheme used to characterize the laminar fabric microarchitecture resulted in an FE mesh with a single element through the thickness of the model, convergence tests were performed to evaluate the numerical accuracy of the mesh. These tests were performed on models with isotropic descriptions of the LC and sclera with multiple elements through the thickness of the LC and confirmed that the meshes were suitably accurate for our analysis of IOP-induced deformation of the LC.

A series of analyses were run for each eye, with a range of values used for the laminar material constant A to determine the effect of this intrinsic material parameter on the mechanical response of the models. With all other variables fixed, including those of the sclera (as described earlier), A was varied to simulate laminar material properties that ranged from highly compliant to highly stiff while maintaining the same relative LC regional anisotropy and inhomogeneity. Note that even for the largest values of A used in the these analyses (800 MPa),

after CTVF and anisotropy were accounted for by equation 1, the corresponding homogenized elastic modulus in the principal orientation for each LC element was approximately an order of magnitude lower than the isotropic modulus used for the sclera.

Two measures of laminar deformation were used to characterize the effect of A on the structural response of the LC: the mean net displacement of the anterior laminar surface and the mean scleral canal expansion. Both of these parameters are measureable using histomorphometry within the 3-D ONH reconstructions produced by our group[32,45] and are therefore potentially useful for model validation against experimental data. The mean net laminar displacement was calculated for each model by fitting a least-squares plane to the anterior laminar insertion, defined as the anterior periphery of the LC where the lamina tethers into the peripapillary sclera. The net anterior–posterior displacement of the anterior LC surface was computed as the mean difference in distance from this plane to the nodes on the anterior LC surface before and after IOP elevation. Similarly, the mean scleral canal expansion of the anterior laminar insertion (ALI) was calculated by first determining the centroid of the scleral canal before and after IOP elevation (via fitting a least-squares ellipse to the nodes along the ALI) and then calculating the mean change in distance from the centroid to each of the anterior laminar insertion nodes at each load state. A similar calculation was performed for the nodes of the posterior laminar insertion (PLI).

In addition to the displacement-based output measures, strain and stress responses within the LC were considered. The regional strain and stress environment was characterized in the LC by grouping elements into superior, inferior, nasal, temporal, and central zones (Fig. 2) and calculating the volume-averaged first principal strain (i.e., the mean tensile strain) and von Mises stress for each region, as well as an overall volume-averaged strain and stress across all elements. Regional CTVF was also compiled for each eye, using the same regionalization scheme.

Intereye Differences in FE Model Output Parameters within Each Animal

To assess the relative intereye variation in mechanical response for the models studied, a specific value for the laminar material constant was prescribed (A = 400 MPa) based on the similarity of net laminar displacement predicted by the models to experimentally measured net laminar displacement.[21] The intereye differences in regional and overall mechanical response as quantified by net laminar displacement, canal expansion, strain, and stress outcome measures were calculated by converting all left eye data to right eye configuration and subtracting the larger value from the smaller value. A percent difference was calculated as the difference between the two eyes divided by the mean of the measurements of the two eyes. From these calculations for each animal, a range of mechanical response variation within contralateral eyes and across animals was established. The variation in CTVF within contralateral eye pairs was also tabulated in this manner.

Results

Predicted Laminar Displacement

A representative plot of net displacement of the anterior LC surface as a function of the laminar material constant A is shown in Figure 3 for both eyes of monkey 2. Note that all contralateral eyes exhibited this characteristic laminar displacement over a range of A values. As shown in the plot, very low values of A (a compliant lamina) produced a large posterior displacement of LC surface relative to the ALI. As the laminar stiffness increased, posterior LC displacement tapered off quickly and for large values of A (a stiff lamina), the LC surface displaced in the anterior direction. This net anterior displacement occurred in stiff LCs because the LC itself deformed very little posteriorly, but instead was pulled taut as the scleral canal expanded.

The color fringe plots of the global displacement for this pair of eyes further illustrate this phenomenon: As the eye expanded under increased IOP, the lamina tilted as it was carried posteriorly within the scleral shell. Simultaneously, the lamina deformed within the canal in a manner dependent on its intrinsic stiffness. When the lamina was highly compliant, it tended to bulge posteriorly, resulting in a large mean value of the net laminar displacement—that is, the mean displacement of the anterior LC surface relative to the ring defining its insertion into the peripapillary scleral was posterior, away from the vitreous (Fig. 3, top left images). Conversely, when the lamina was stiff (but still approximately an order of magnitude less stiff in its principal direction than the isotropic stiffness of the surrounding sclera), it tautened and warped in such a way that the average net movement relative to the ALI was anterior (Fig. 3, top right images). These two modes of laminar deformation— bulging or tautening—and their relative magnitudes underlie the net average anterior or posterior displacement, respectively, of the LC plotted in the graph of Figure 3.

In Table 1, net laminar displacement is shown for all four pairs of eyes when the laminar material constant was set to 400 MPa. This value of A produced small net posterior displacement predictions between 0 and 13 μm for all FE models. These magnitudes match well with experimental data showing that the LC deformed up to 8 μm posteriorly and 11 μm anteriorly in six pairs of bilaterally normal monkeys in which one eye was perfusion fixed at an IOP of 10 mm Hg, and the contralateral eye at 45 mm Hg.[21]

Predicted Scleral Canal Expansion

A representative plot of scleral canal expansion at the ALI and PLI in monkey 2 is shown in Figure 4. This outcome measure was less sensitive to the laminar material constant A than was the net laminar displacement, but did exhibit the same trend (i.e., more compliant lamina resulted in greater canal expansion). This plot also shows that the amount of PLI expansion was larger than ALI expansion over the entire range of A, a behavior that was consistent across all models analyzed (Table 1) but occurred in only three of six eye pairs in previously published data.[21] Scleral canal expansion predictions for all four pairs of eyes at a laminar material constant value of 400 MPa are also presented in Table 1. The scleral canal expansion predictions showed remarkable similarity between contralateral eyes at A = 400 MPa, where percent differences ranged from less than 1% to 6%. This similarity in mechanical response over a range of laminar stiffnesses is further exemplified in Figure 4.

Predicted Laminar Strain and Stress

Plots of strain versus the laminar material constant A are presented for monkey 2 in Figure 5. As laminar stiffness increased, the predicted maximum principal (tensile) strains within the LC decreased nonlinearly. This trend held for both the median and the upper and lower ranges within the laminar elements. Color fringe plots for this monkey indicated that the highest tensile strains were concentrated in the temporal region of the LC. Compiled strain data for all eyes (Table 1) also support the temporal region as a high strain environment for most of the eyes modeled. Comparison of the fringe plots of strain to global displacement also confirmed that the regions of largest strains do not necessarily correlate with the regions of largest displacement (Figs. 3, 4). This underscores the concept that strain is a measure of relative deformation, similar to stretch, whereas displacement is simply a measure of positional change.

Figure 6 shows the corresponding plots of stress as a function of the laminar material constant A in monkey 2. These

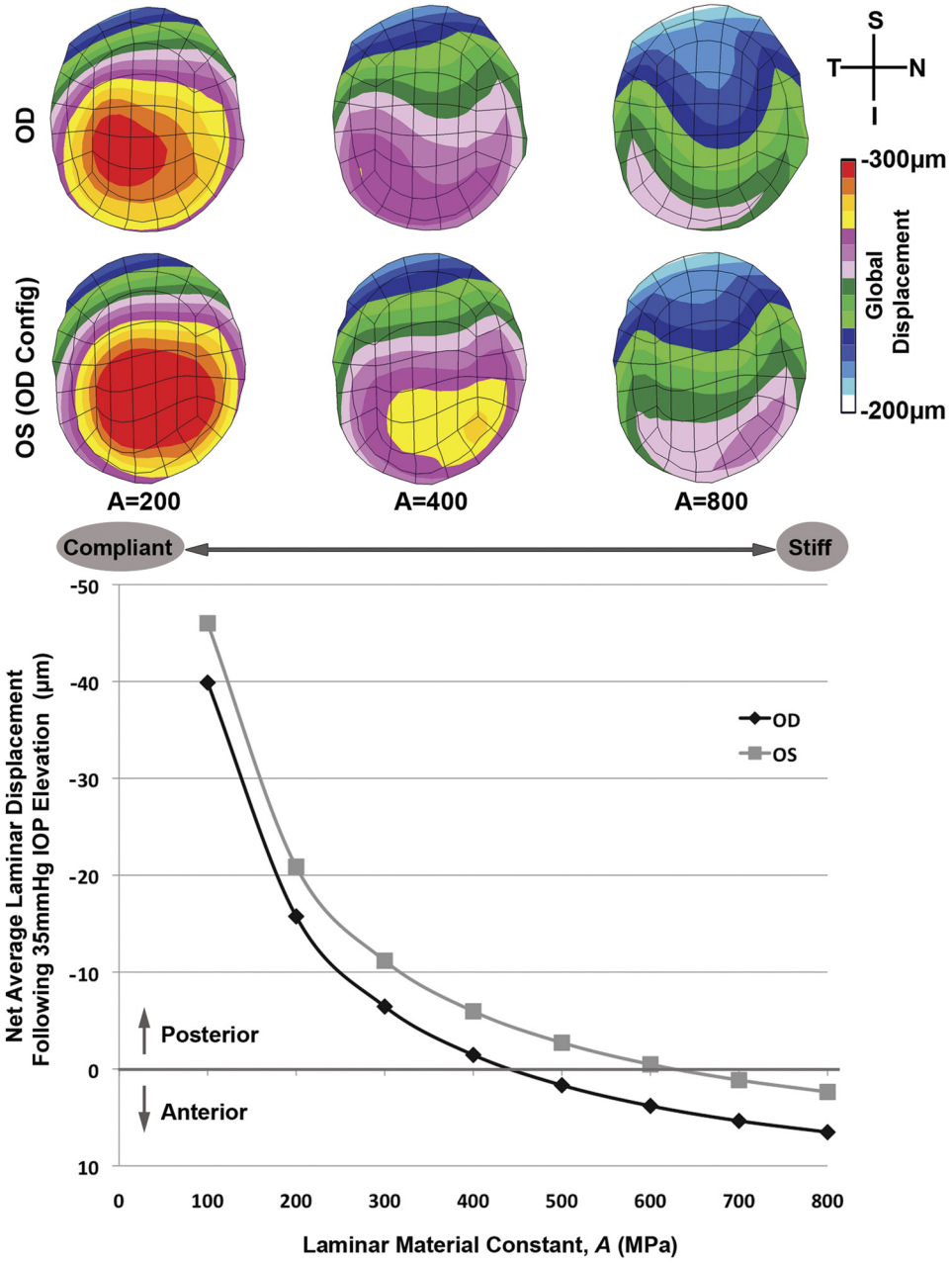

FIGURE 3. Displacement behavior of the LC in monkey 2 as a function of the laminar material constant *A*. The fringe plots of global displacement show that for all values of *A*, the inferior aspect of the lamina tended to tilt more posteriorly than the superior aspect when IOP was increased (as indicated by the overall superior-to-inferior gradient of the displacement). When the lamina was compliant (i.e., *A* was small), a large central portion of it bulged posteriorly in a cupped shape, so that the average net displacement relative to the anterior laminar insertion (ALI) was relatively large (see graph). When the lamina was stiff (i.e., *A* was large) this posterior bowing was largely absent and the central portion exhibited anterior displacement as the lamina was pulled taut and warped. The net average displacement of the laminar surface relative to the ALI in this case was in the anterior direction.

plots show that as laminar stiffness increased, the stress within the LC increased linearly as the LC bore more load. Furthermore, larger values of the laminar material constant led to wider ranges of stress values within the LC (i.e., a less uniform stress distribution). Stress was highest in the central region in all but one of the eyes studied (Table 1).

The color fringe plots in Figures 5 and 6 along with the data of Table 1 also illustrate that both the patterns and magnitudes of strain and stress within the LC were remarkably similar in contralateral eyes. The maximum percent difference between corresponding regions in contralateral eyes ranged from 7% to 38% and 11% to 22% for strain and stress, respectively (Table 1). The relative differences between contralateral eyes in overall strain and stress ranged from 1% to 23% and 6% to 17%, respectively. Across animals, strain and stress magnitude showed larger variation. For example, the strain in the temporal region of the right eye of monkey 1 was 2.07% while it was 0.92% in the left eye of monkey 4, a 76% difference. Similarly, the stress magnitudes for the same comparison were 14.3 and 26.4 kPa, a difference of 59%.

Correlation between CTVF and Strain and Stress

The regional analysis data presented in Table 1 also showed that the highest strains and lowest stresses were concentrated in the areas with the lowest CTVF (primarily temporal). Conversely, the highest stresses and lowest strains were associated with regions with the highest CTVF (primarily central and superior). In Figure 7, the CTVF associated with the underlying microstructure for each of the 45 LC FE volumes was plotted versus its element averaged strain or stress value. These plots confirm that the models' predicted strain is inversely related to CTVF and that the relationship is well represented by a power law relationship: r^2 ranged from 0.45 to 0.82 with a median r^2 for all eyes of 0.73. The von Mises stress was linearly correlated with CTVF and

TABLE 1. Predicted Displacement, Strain, and Stress for All Models with the Laminar Material Constant Set at A = 400 MPa

Outcome Measure	Monkey 1				Monkey 2				Monkey 3				Monkey 4			
	OD	OS	Max-Min	% Diff	OD	OS	Max-Min	% Diff	OD	OS	Max-Min	% Diff	OD	OS	Max-Min	% Diff
Avg LC displacement, μm	−12.8	−2.1	10.67	144	−1.4	−6.0	4.51	122	−9.8	−5.5	4.34	57	−4.1	−0.4	3.63	162
ALI expansion, μm	24.5	23.4	1.05	4	19.0	18.8	0.23	1	16.6	16.9	0.28	2	20.6	21.0	0.38	2
PLI expansion, μm	30.8	28.9	1.86	6	24.9	25.2	0.32	1	26.3	24.9	1.39	5	24.7	24.8	0.10	0

Parameter	Region	Monkey 1				Monkey 2				Monkey 3				Monkey 4			
		OD	OS	Max-Min	% Diff	OD	OS	Max-Min	% Diff	OD	OS	Max-Min	% Diff	OD	OS	Max-Min	% Diff
Maximum principal strain, %	Overall	1.35	1.07	0.28	23	1.00	1.05	0.05	5	1.00	0.98	0.03	3	0.91	0.92	0.01	1
	Superior	1.09	0.96	0.13	13	0.84	0.82	0.02	2	0.80	0.89	0.09	11	0.83	0.84	0.01	1
	Nasal	1.40	1.15	0.25	20	1.11	1.24	0.13	11	1.12	0.96	0.17	16	0.94	1.01	0.07	7
	Inferior	1.11	0.97	0.15	14	0.91	1.12	0.21	20	0.96	0.93	0.03	3	0.95	0.96	0.01	1
	Temporal	2.07	1.41	0.66	38	1.30	1.27	0.03	2	1.21	1.19	0.03	2	0.93	0.92	0.00	0
	Central	1.07	0.87	0.19	20	0.83	0.80	0.03	4	0.92	0.91	0.01	1	0.89	0.87	0.02	2
VonMises stress, kPa	Overall	18.2	19.2	1.06	6	18.0	16.4	1.53	9	13.4	15.9	2.43	17	22.7	24.1	1.41	6
	Superior	17.7	18.6	0.87	5	14.9	14.6	0.34	2	12.0	14.5	2.41	18	21.8	24.3	2.46	11
	Nasal	17.9	19.4	1.57	8	18.7	16.1	2.67	15	12.2	15.3	3.09	22	20.3	21.0	0.70	3
	Inferior	17.7	19.7	2.03	11	17.5	15.1	2.41	15	11.4	13.4	1.99	16	20.4	22.7	2.32	11
	Temporal	14.3	15.2	0.84	6	18.0	15.4	2.67	16	14.7	17.1	2.39	15	24.6	26.4	1.88	7
	Central	23.2	23.2	0.01	0	20.6	21.1	0.45	2	16.8	19.1	2.29	13	26.2	25.9	0.27	1
CTVF	Overall	0.21	0.23	0.02	9	0.23	0.22	0.01	4	0.20	0.23	0.03	14	0.26	0.27	0.01	4
	Superior	0.24	0.24	0.00	0	0.22	0.22	0.00	0	0.22	0.23	0.01	4	0.27	0.29	0.02	7
	Nasal	0.20	0.22	0.02	10	0.22	0.19	0.03	15	0.19	0.21	0.02	10	0.24	0.25	0.01	4
	Inferior	0.20	0.22	0.02	10	0.22	0.19	0.03	15	0.18	0.23	0.05	24	0.25	0.25	0.00	0
	Temporal	0.15	0.18	0.03	18	0.19	0.19	0.00	0	0.19	0.21	0.02	10	0.26	0.28	0.02	7
	Central	0.25	0.28	0.03	11	0.26	0.27	0.01	4	0.23	0.24	0.01	4	0.29	0.28	0.01	4

Regional CTVF values are also reported for comparison to strain and stress values. Regions of maximum and minimum strain, stress, and CTVF are highlighted to draw attention to the relationships between underlying microarchitecture and mechanical strain and stress found in these models.

regional maximum.

regional minimum.

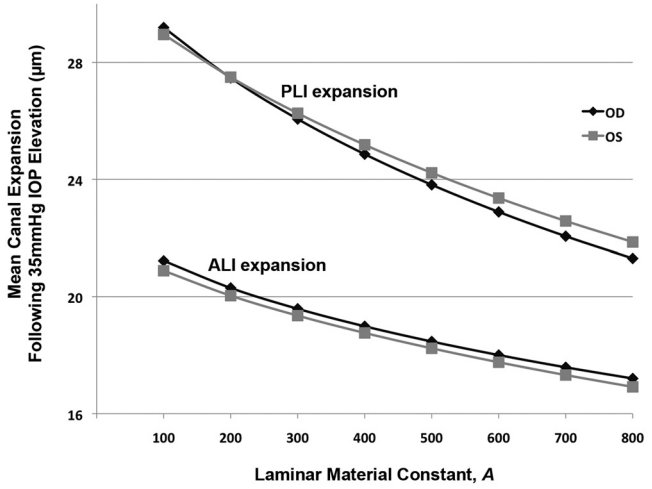

FIGURE 4. Predicted scleral canal expansion at the anterior and posterior laminar insertions (ALI and PLI, respectively), due to an IOP elevation of 35 mm Hg as a function of the laminar material constant *A* in monkey 2. Expansion of the scleral canal at the PLI was always greater than at the ALI and was more sensitive to the stiffness of the lamina. The contralateral symmetry of mechanical response for scleral canal expansion was evident.

linear regressions that were constrained to impose a *y*-intercept of 0 produced correlations with r^2 between 0.31 and 0.82 and a median r^2 for all eyes of 0.63.

DISCUSSION

In this report, we present biomechanical FE models of the posterior pole of the eye that incorporate local laminar stiffnesses that reflect the underlying microarchitecture of the LC connective tissues. These models translate beam- and pore-level characteristics of the LC, specifically the connective tissue volume fraction and the predominant orientation of the laminar beams, into a locally homogenized description of the directional stiffness. The mechanical properties defined through this translation included the specification of an intrinsic material constant *A* for the LC tissue. Using models developed from four pairs of bilaterally normal monkey eyes, we investigated the effect of the magnitude of this laminar material constant on the biomechanical behavior of the models by characterizing the predicted global and relative displacements of the LC and the scleral canal, along with the overall and regional stresses and strains throughout the LC. We also examined the degree of mechanical response similarity between contralateral eyes and investigated the relationship between LC microarchitecture and strain and stress.

Our models predict that the net movement of the LC under acute IOP elevation can be either anterior or posterior, depending on whether the value of the laminar material constant is high or low, respectively, but that the magnitude of potential anterior movement is much lower than posterior movement. Our models also predict modest scleral canal expansion, with the PLI consistently expanding by a greater amount than the ALI for a given laminar stiffness. Scleral canal expansion was only moderately dependent on the laminar material constant. Strains within the LC were inversely related to the value of the laminar material constant and spanned a wider range when the LC was more compliant. The opposite relationships held for the stresses within the LC. Strains and stresses were comparable between contralateral eyes with the magnitude of the regional maximum difference between contralateral eyes ranging from 7% to 38% and 11% to 22%, respectively, across the four animals. The highest strains and lowest stresses predicted by the models occurred in regions of lowest CTVF (primarily temporal). Conversely, the highest stresses and lowest strains were concentrated in regions of highest CTVF (primarily central and superior). Strains within the entire LC showed a nonlinear negative correlation with underlying CTVF. Stresses within the LC were positively and linearly correlated to local CTVF, but to a somewhat lesser degree than the strain relationship.

Our results confirm that the anatomic similarity in contralateral monkey eyes translates into bilaterally similar mechanical behavior despite some differences in LC connective tissue distribution and beam arrangement.[27] They also show that the variability of mechanical response between animals is much greater than the variability between contralateral eyes. As such, these results represent a first step in establishing a range of physiologic variability of the mechanical environment within FE models of the monkey LC. Furthermore, they bolster the strength and utility of intereye comparisons of mechanical environment, an important consideration for investigations in which one eye is subject to experimental perturbation and undergoes subsequent changes in laminar geometry and microarchitecture (e.g., induction of experimental glaucoma in one eye in which the LC subsequently remodels into a new configuration).

The FE models presented herein suggest that the magnitude and direction (anterior or posterior) of LC surface displacement relative to the anterior lamina insertion depends, in part, on the material stiffness assigned to the LC through the global laminar material constant, *A*. This possibility agrees with experiments in monkey eyes that have shown via a 3-D histomorphometric technique that acute IOP elevation from 10 to 45 mm Hg produces average LC displacement in both the anterior and posterior direction.[21] The most interesting finding of those experiments is that average IOP-induced LC displacement is relatively small—a maximum of 11 and 8 μm in the anterior and posterior directions, respectively—and varies between animals.[21] This result agrees with recently presented in vivo spectral domain OCT imaging data from human eyes (Agoumi Y et al. IOVS 2009;50:ARVO E-Abstract 4898). Posterior displacement of the LC has been presumed to be the primary form of laminar displacement under acute IOP elevation, as this direction is congruent with the eventual direction of cupping and excavation phenomena seen in advanced human glaucoma. The notion of acute anterior movement of the LC has received less attention, perhaps because this type of laminar displacement is less intuitive. Bellezza et al.[46] observed substantial anterior LC movement when histologically comparing a group of immersion fixed, nonpressurized eyes with perfusion fixed eyes at IOP of 10 mm Hg. In that study, the anterior movement of the LC was presumably due to a true tautening of the lamina as it transitioned from an unloaded structure hanging within the neural canal to an engaged, loaded structure at an IOP of 10 mm Hg. Sigal et al.[20] also observed the potential for net anterior displacement of the LC under elevated IOP using eye-specific FE models of human tissues with homogeneous isotropic material descriptions of the LC and sclera. In their modeling study, this anterior movement of the LC occurred when simulating an increase in IOP.

In all the models presented herein, expansion of the scleral canal at the PLI was always larger than that at the ALI. Recent 3-D histomorphometric measurements from acute IOP elevation experiments showed greater scleral canal expansion at the PLI than at the ALI in half of the measured eyes, but nearly

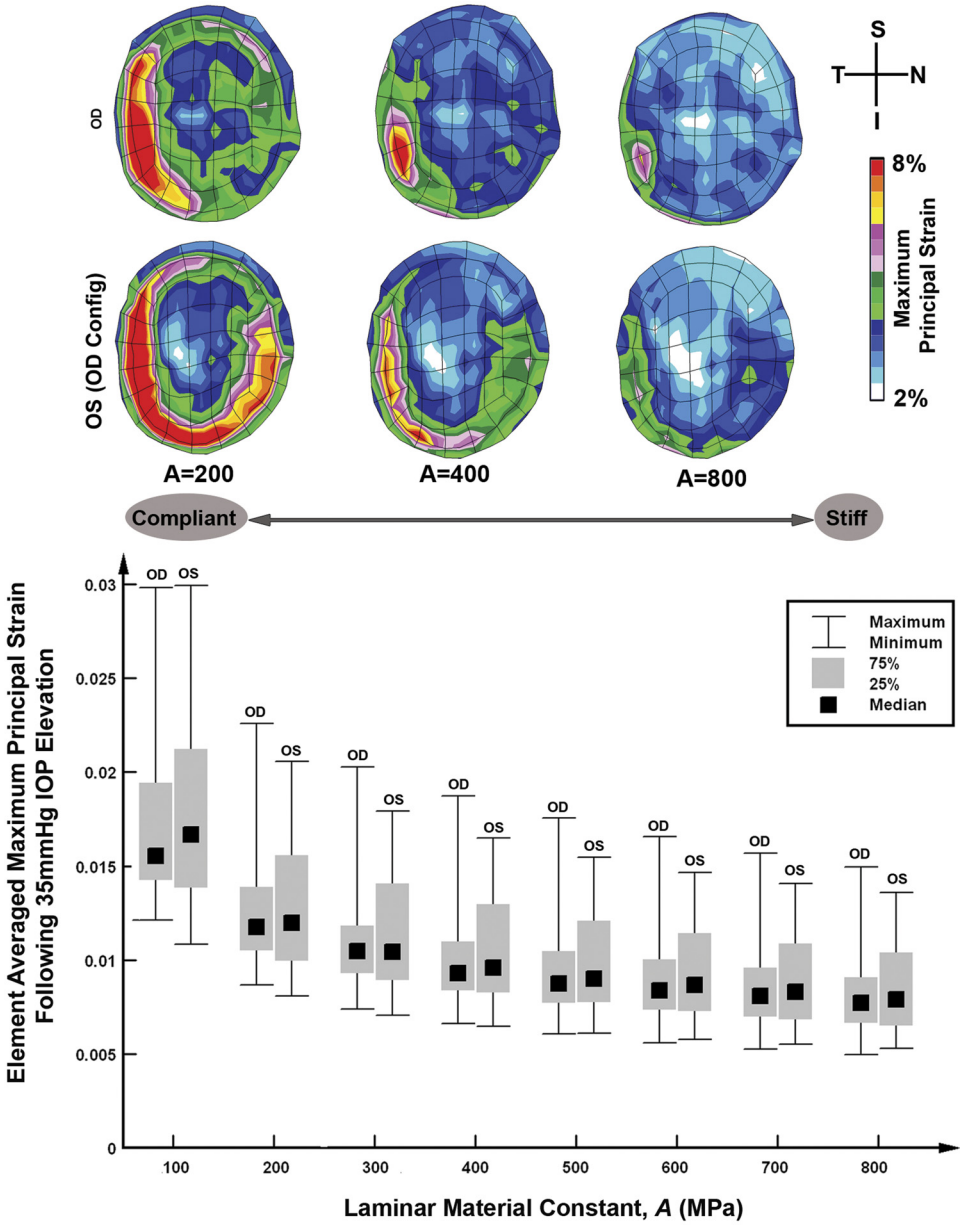

FIGURE 5. Elemental mean maximum principal strains in monkey 2 as a function of the laminar material constant A for both the left and right eyes. A box plot is used to show the range of average elemental strains over the 45 elements of the LC. Note the similarity in strain distributions for this pair of eyes over the range of laminar stiffness constant considered.

equal amounts of expansion in the remainder of the eyes.[21] The ALI and PLI expansion data in the experimental data also exhibited a wider variability than model predictions (−20 to 13 μm at the ALI and −21 to 31 μm at the PLI). The underlying reasons for this discrepancy deserve additional attention in future work. It is possible that our use of linear isotropic material properties for sclera is inadequate to capture more complex canal deformation.

It is important to appreciate the underlying mechanical, geometric, and material factors that govern the net direction of movement of the LC connective tissues under acute IOP elevation. We have previously described the deformation of the lamina as being influenced by two simultaneous loading conditions: the direct action of IOP on the neural tissue encapsulating the LC that tends to push the LC posteriorly, and the hoop stress engendered by IOP and borne in the peripapillary sclera that tends to expand the neural canal, acting to pull the LC taut and displace the LC surface in the anterior direction.[10,46] The magnitude and direction of the net laminar displacement for a given IOP will depend on both the geometric details the ONH anatomy (e.g., LC thickness and mean laminar position) and the interplay between the structural stiffnesses of the sclera and LC. From a geometric perspective, an eye with a relatively flat LC (i.e., in-plane with the surrounding peripapillary sclera) would have much less propensity to move anteriorly under IOP elevation compared with one with a naturally deeper LC shape. From a material property perspective, our eye-specific models suggest that if the lamina is compliant enough (i.e., has a low A value) it can be expected to undergo posterior displacement.[21] It is possible that such material stiffness-related phenomena underlies the occasional hypercompliance we have observed in earlier studies of early experimental glaucoma in the monkey.[47] Similarly, a stiffer lamina (i.e., high value of A) can be expected to deform much less posteriorly and even displace anteriorly, albeit by a small magnitude. Tissue-level changes in the sclera and LC that reduce compliance, as might occur in age-related collagen cross-linking or pathologic remodeling or scarring of laminar tissues,[48,49] should be expected to change the overall characteristics of IOP-induced LC deformation, stress, and strain. Hence, charac-

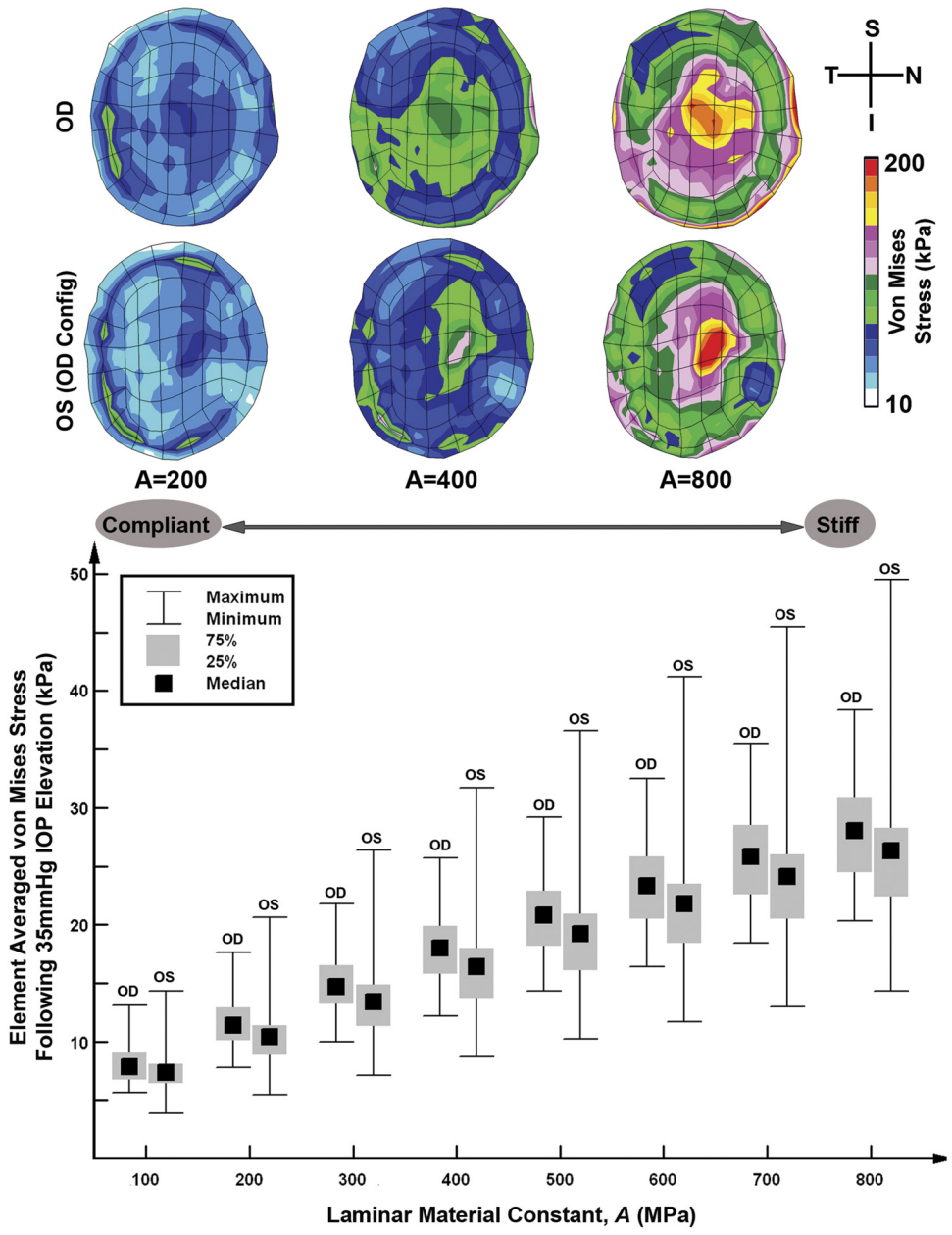

FIGURE 6. Elemental von Mises stresses as a function of the laminar material constant *A* for both the left and right eyes of monkey 2. A box plot is used to show the range of average elemental stresses over the 45 elements of the LC.

terization of the nature of laminar and peripapillary scleral connective tissue displacement and expansion under acute IOP elevation may provide an indicator of connective tissue health, disease, or susceptibility to glaucomatous damage.

To this end, we suggest that while strain is likely to be the most relevant mechanical factor for quantifying tissue-level insult or perturbation of the astrocytes' mechanical milieu, measurement of laminar displacement and canal expansion are also relevant and important because they represent realistic imaging targets for future devices designed probe the deeper connective tissues of the ONH. To date, the inaccessibility of the ONH connective tissues has hampered efforts to directly measure and characterize the mechanical response of the LC to acute IOP elevation, either in vivo or ex vivo. Scanning laser ophthalmoscopy has been used to assess laminar position and pore size and shape in vivo by imaging the most superficial LC beams in normal and glaucomatous eyes,[50–52] but the acute response of these imaging targets to elevated IOP has not been explored. However, ex vivo imaging of pore size changes under acute IOP elevation has been obtained using second harmonic imaging.[53,54] Ex vivo measures of laminar deformation and neural canal expansion have been reported in individual eyes using x-ray based techniques,[55] individual immersion and perfusion fixed monkey eyes,[46] and within contralateral eyes fixed at two different pressures with 2-D histologic[47,56] and 3-D histomorphometric techniques.[21] Laser scanning confocal microscopy of laminar connective tissue has been used to characterize the volumetric distension and laminar surface strain over a range of applied pressures in an ex vivo preparation.[48] Direct in vivo imaging by spectral domain and ultrahigh-speed optical coherence tomography shows considerable promise for viewing the LC in 3-D[57,58] and its application in acute pressure elevation experiments is being investigated (Burgoyne CF, et al. *IOVS* 2007;46:ARVO E-Abstract 3296).[59]

We suggest that future developments and refinements in deep-scan OCT and second harmonic imaging technologies

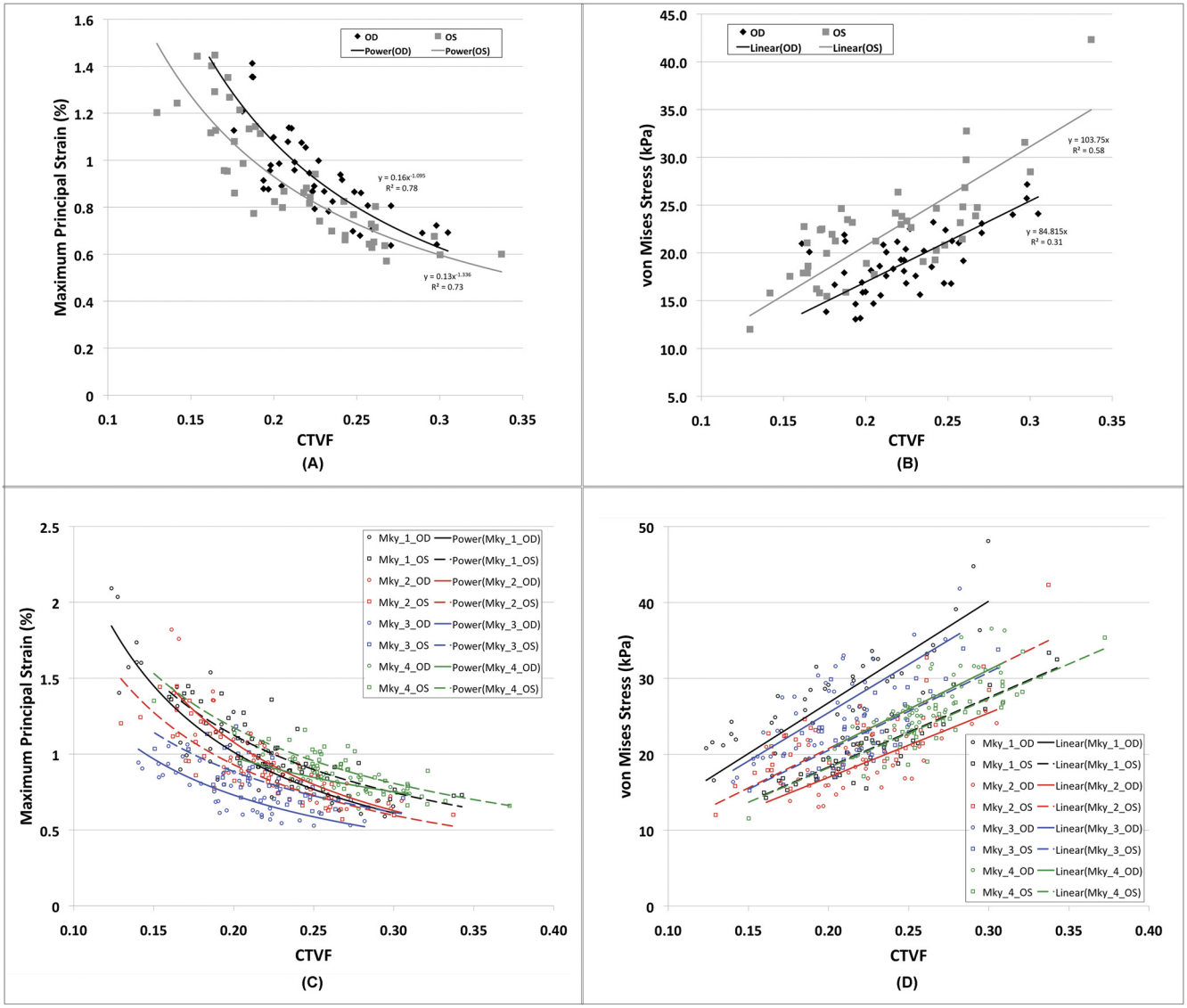

Figure 7. The relationship between CTVF and maximum principal strain and von Mises stress. Each data point represents the element-averaged value of stress or strain for a given LC element, and each LC element's CTVF is characterized as described in Roberts et al.[27] For these plots, the laminar material constant was adjusted until a net 0 displacement of the anterior LC surface was produced for an IOP elevation of 35 mm Hg. (**A**) The relationship between CTVF and maximum principal strain in monkey 2 has a negative correlation and is best fit using a power law relationship. (**B**) The CTVF and von Mises stress in monkey 2 is positively correlated and is best fit by using a linear relationship constrained to have a 0 *y*-intercept. (**C**) Maximum principal strain versus CTVF for all pairs of eyes with associated nonlinear curve fits. (**D**) von Mises stress versus CTVF for all pairs of eyes with associated linear curve fits.

will provide much-needed data concerning the mechanical response to the load-bearing tissues of the ONH to acute IOP elevation. Indeed, future refinement of material constitutive relationships and validation of FE models will require such techniques to allow in vivo measurement of the load-deformation response of the laminar and peripapillary tissues. More important, characterization of the nature of LC and peripapillary sclera connective tissue deformation under acute IOP elevation in concert with suitable biomechanical models could play an important role in developing a clinical approach for assessing individual susceptibility to glaucoma or the stage of glaucomatous progression in patients.

The FE models predicted an inverse relationship between laminar CTVF and tensile strain, with the less dense temporal region being subjected to the highest strains and the more robust central and superior regions bearing the lowest strains. This relationship is intuitive in that regions of the LC with a lower connective tissue density would be expected to undergo greater stretching during IOP elevation provided that stress transmission throughout the LC is roughly uniform. An interesting aspect of the power–law relationship we found between strain and CTVF is that for low values of CTVF, the local strain is highly dependent on CTVF, but at high CTVF, its influence of CTVF on strain diminishes (Figs. 7A, 7C). It should be noted, however, that this result is intimately tied to the microstructure-to-stiffness relationship of equation 1. Thus, until this strain-CTVF relationship can be directly verified experimentally, the importance of this computational result remains unconfirmed. If the relationship can be verified, characterization of CTVF variation in the lamina may become a powerful surrogate measure for the mechanical strain field in the LC and could provide important insight into associated strain-mediated phenomena such as axonal distress, axonal transport blockade, astrocyte activation, tissue damage, and remodeling.

It should be noted that the strains calculated with the current models are continuum-level measures and therefore represent a bulk description of strain within the microstructure rather than the amount of strain within the individual laminar beams. We suspect that the strains within the family of beams subtended by an elemental volume are quite variable, but that the largest concentration of high-strain laminar beams is still located in the temporal quadrant where continuum-level strains are highest. Hence, the strain and stress measures reported here should be regarded as homogenized quantities from which overall regional relationships may be observed. Techniques for modeling the beam level stress and strain environment are under active development and will be the subject of future reports (Downs J, et al. *IOVS* 2007;46:ARVO E-Abstract 3301; Kodiyalam S, et al. *IOVS* 2008;47:ARVO E-Abstract 3667).[60]

With respect to the anatomy represented in the FE models of this report, neither the retrolaminar septa nor the pia mater were included in the analyses. In a previous report, we showed that in early experimental glaucoma, retrolaminar septa appear to be remodeled into load-bearing tissue that is morphologically similar to and contiguous with the LC.[27] It is possible that the retrolaminar connective tissue structures play a more important role in load-bearing than heretofore appreciated, particularly during the early phases of extracellular matrix remodeling. It is also possible that these retrolaminar tissues underlie some of the aforementioned differences in canal expansion behavior we observed between our FE models and 3-D histomorphometric measurements of acute IOP-related deformations.[21] As our understanding of the acute mechanical response of the ONH to IOP advances, it may be necessary to account for retrolaminar tissues in future FE models.

It is also important to point out several of the assumptions inherent in the material property definitions used herein and highlight the potential limitations that they impose. First, we have modeled the sclera as a linear isotropic material based on uniaxial stress relaxations tests performed previously. However, it has been shown through uniaxial testing that the sclera is nonlinear, and more recent inflation testing has characterized the anisotropic nonlinearity of sclera, particularly in the peripapillary sclera where fiber orientation is strongly circumferential.[35,61–63] Neglect of these aspects of the scleral material properties may cause our models to impart unrealistic scleral deformations, stresses, and strains to the LC. Hence, our laminar structures may be more shielded from the effects of in-wall hoop stress than would be the case had these material characteristics been taken into account. Furthermore, our models neglect the possible presence of prestresses within the tissue, even though they are fixed at 10 mm Hg. Despite these issues, the scleral canal expansions predicted by the models presented herein (and transmitted to the contained LC) are well within the range of the canal expansions observed experimentally,[21] and so we believe the results reported herein are robust to these assumptions.

A second assumption in our material property definition is the use of the phenomenologic relationship of equation 1 to convert microarchitectural information into continuum-level material properties. While this relationship allows for material anisotropy to be imparted to elemental regions of the LC, this material symmetry is assumed to be orthotropic (i.e., there are up to three mutually perpendicular directions of principal stiffness), an assumption that may not be strictly true. Moreover, the functional form of the microstructure-to-stiffness relationship in equation 1 has not been experimentally verified for LC tissue. Power law relationships have historically been used to relate density to material properties in porous foams,[37,38] and the particular form incorporating anisotropy used in the present study was adopted from the literature related to trabecular bone mechanics.[36] Although we acknowledge that the material properties for bone differ substantially from the soft connective tissue structure of the LC, the formulation was adopted based on the similarity in these tissues' microarchitecture. Furthermore, our current level of modeling sophistication for the LC treats it as a linear material. The incorporation of measurable aspects of the microarchitecture (i.e., local inhomogeneity and anisotropy) into FE models of the LC is a significant refinement over approaches that consider the lamina to be a homogeneous linearly isotropic structure,[20,24,26] but further work is clearly needed to develop a better constitutive description of the LC. At the present time, the experimental data required to formulate an appropriate LC microarchitecture-stiffness relationship and validate it with pressure-displacement data do not exist. Imaging techniques such as second harmonic imaging, confocal microscopy, and deep scan OCT may prove useful for characterizing such load-deformation characteristics of the LC, but the technical challenges associated with performing these measurements and relating them to a material stiffness model are not easily overcome.

Another aspect of the assumed microstructure-to-stiffness relationship is that the resultant material properties of the LC are implemented as linear orthotropic materials rather than nonlinear. One consequence of this linearity is that for very low values of A the net laminar displacement becomes unrealistically large, since no stretch-induced stiffening of the tissue is simulated (Fig. 3). In our analyses, we have used a geometric nonlinearity solution approach to account for large strains that occur in the analysis, but we have not provided for a nonlinear constitutive model. Furthermore, even with the constitutive relationship of equation 1, it is unclear how an appropriate value should be assigned to A for each individual eye in the absence of direct testing of each model's IOP–deformation response against experimental measures. Once experimental techniques that allow mechanical testing and imaging of laminar tissue over a range of IOPs become available, it will be possible to determine whether a nonlinear material model for the LC tissue is warranted and a more comprehensive approach for selecting model constants will emerge.

Despite these limitations, the work presented herein establishes a method for incorporating eye-specific LC microarchitectural information into biomechanical models of the posterior pole. These models demonstrate the biomechanical behavior of the peripapillary sclera and LC over a wide range of LC stiffnesses and establish strong spatial relationships between local LC connective tissue density and local stress and strain. These models characterize the macroscale mechanical environment of the ONH exposed to acute IOP elevations in the normal monkey eye and will also be helpful for understanding the mechanical consequences of connective tissue remodeling that we have shown to be associated with experimental glaucoma in the monkey.[27,32,45,64] This work emphasizes that measurement of overall LC surface deformation (not to be confused with the ONH surface deformation) is insufficient to predict regional laminar strain and stress, both of which are likely to be important contributors to local IOP-related glaucomatous damage. As such, these results highlight the importance of developing new imaging modalities to characterize the acute IOP-induced deformation response of the LC microstructure as a possible surrogate measure for local stress and strain. Progress in such imaging approaches will allow for additional refinements and validation of these and other FE models, which in turn will be useful for identifying correlations between the mechanical environment of the ONH and acute and longer term tissue responses.

Acknowledgments

The authors gratefully acknowledge the contributions made by Budd Hirons and Pris Zhou.

References

1. Quigley HA, Broman AT. The number of people with glaucoma worldwide in 2010 and 2020. *Br J Ophthalmol.* 2006;90:262–267.
2. Mozaffarieh M, Grieshaber MC, Flammer J. Oxygen and blood flow: players in the pathogenesis of glaucoma. *Mol Vis.* 2008;14:224–233.
3. Resch H, Garhofer G, Fuchsjager-Mayrl G, Hommer A, Schmetterer L. Endothelial dysfunction in glaucoma. *Acta Ophthalmol.* 2009;87:4–12.
4. Gupta N, Yucel YH. Glaucoma as a neurodegenerative disease. *Curr Opin Ophthalmol.* 2007;18:110–114.
5. Investigators TA. The advanced glaucoma intervention study (AGIS): 7. The relationship between control of intraocular pressure and visual field deterioration. *Am J Ophthalmol.* 2000;130:429–440.
6. Kass MA, Heuer DK, Higginbotham EJM, et al. The Ocular Hypertension Treatment Study: a randomized trial determines that topical ocular hypotensive medication delays or prevents the onset of primary open-angle glaucoma. *Arch Ophthalmol.* 2002;120:701–713.
7. Leske MC, Heijl A, Hussein M, Bengtsson B, Hyman L, Komaroff E. Factors for glaucoma progression and the effect of treatment: the early manifest glaucoma trial. *Arch Ophthalmol.* 2003;121:48–56.
8. Anderson DR, Drance SM, Schulzer M. Factors that predict the benefit of lowering intraocular pressure in normal tension glaucoma. *Am J Ophthalmol.* 2003;136:820–829.
9. Bellezza AJ, Hart RT, Burgoyne CF. The optic nerve head as a biomechanical structure: initial finite element modeling. *Invest Ophthalmol Vis Sci.* 2000;41:2991–3000.
10. Downs JC, Roberts MD, Burgoyne CF. Mechanical environment of the optic nerve head in glaucoma. *Optom Vis Sci.* 2008;85:425–435.
11. Quigley HA, Addicks EM, Green WR, Maumenee AE. Optic nerve damage in human glaucoma. II. The site of injury and susceptibility to damage. *Arch Ophthalmol.* 1981;99:635–649.
12. Burgoyne CF, Downs JC, Bellezza AJ, Suh JK, Hart RT. The optic nerve head as a biomechanical structure: a new paradigm for understanding the role of IOP-related stress and strain in the pathophysiology of glaucomatous optic nerve head damage. *Prog Retin Eye Res.* 2005;24:39–73.
13. Coleman AL, Quigley HA, Vitale S, Dunkelberger G. Displacement of the optic nerve head by acute changes in intraocular pressure in monkey eyes. *Ophthalmology.* 1991;98:35–40.
14. Burgoyne CF, Quigley HA, Thompson HW, Vitale S, Varma R. Measurement of optic disc compliance by digitized image analysis in the normal monkey eye. *Ophthalmology.* 1995;102:1790–1799.
15. Burgoyne CF, Quigley HA, Thompson HW, Vitale S, Varma R. Early changes in optic disc compliance and surface position in experimental glaucoma. *Ophthalmology.* 1995;102:1800–1809.
16. Heickell AG, Bellezza AJ, Thompson HW, Burgoyne CF. Optic disc surface compliance testing using confocal scanning laser tomography in the normal monkey eye. *J Glaucoma.* 2001;10:369–382.
17. Morgan WH, Chauhan BC, Yu D-Y, Cringle SJ, Alder VA, House PH. Optic disc movement with variations in intraocular and cerebrospinal fluid pressure. *Invest Ophthalmol Vis Sci.* 2002;43:3236–3242.
18. Hafez AS, Bizzarro RL, Rivard M, Lesk MR. Changes in optic nerve head blood flow after therapeutic intraocular pressure reduction in glaucoma patients and ocular hypertensives. *Ophthalmology.* 2003;110:201–210.
19. Sigal IA, Flanagan JG, Tertinegg I, Ethier CR. Finite element modeling of optic nerve head biomechanics. *Invest Ophthalmol Vis Sci.* 2004;45:4378–4387.
20. Sigal IA, Flanagan JG, Tertinegg I, Ethier CR. Modeling individual-specific human optic nerve head biomechanics. Part I: IOP-induced deformations and influence of geometry. *Biomech Model Mechanobiol.* 2009;8(2):85–98.
21. Yang H, Downs JC, Sigal IA, Roberts MD, Thompson H, Burgoyne CF. Deformation of the normal monkey optic nerve head connective tissue following acute IOP elevation within 3-D histomorphometric reconstructions. *Invest Ophthalmol Vis Sci.* Published online July 23, 2009.
22. Sigal IA, Flanagan JG, Ethier CR. Factors influencing optic nerve head biomechanics. *Invest Ophthalmol Vis Sci.* 2005;46:4189–4199.
23. Sigal IA, Flanagan JG, Tertinegg I, Ethier CR. Reconstruction of human optic nerve heads for finite element modeling. *Technol Health Care.* 2005;13:313–329.
24. Sigal IA, Flanagan JG, Tertinegg I, Ethier CR. Predicted extension, compression and shearing of optic nerve head tissues. *Exp Eye Res.* 2007;85:312–322.
25. Sigal IA, Flanagan JG, Tertinegg I, Ethier CR. Modeling individual-specific human optic nerve head biomechanics. Part II: influence of material properties. *Biomech Model Mechanobiol.* 2009;8(2):99–109.
26. Sigal IA. Interactions between geometry and mechanical properties on the optic nerve head. *Invest Ophthalmol Vis Sci.* 2009;50(6):2785–2795.
27. Roberts MD, Grau V, Grimm J, et al. Remodeling of the connective tissue microarchitecture of the lamina cribrosa in early experimental glaucoma. *Invest Ophthalmol Vis Sci.* 2009;50:681–690.
28. Yang H, Downs JC, Burgoyne CF. Physiologic intereye differences in monkey optic nerve head architecture and their relation to changes in early experimental glaucoma. *Invest Ophthalmol Vis Sci.* 2009;50:224–234.
29. Grau V, Downs JC, Burgoyne CF. Segmentation of trabeculated structures using an anisotropic Markov random field: application to the study of the optic nerve head in glaucoma. *IEEE Trans Med Imaging.* 2006;25:245–255.
30. Downs JC, Blidner RA, Bellezza AJ, Thompson HW, Hart RT, Burgoyne CF. Peripapillary scleral thickness in perfusion-fixed normal monkey eyes. *Invest Ophthalmol Vis Sci.* 2002;43:2229–2235.
31. Downs JC, Ensor ME, Bellezza AJ, Thompson HW, Hart RT, Burgoyne CF. Posterior scleral thickness in perfusion-fixed normal and early-glaucoma monkey eyes. *Invest Ophthalmol Vis Sci.* 2001;42:3202–3208.
32. Yang H, Downs JC, Girkin C, et al. 3-D histomorphometry of the normal and early glaucomatous monkey optic nerve head: lamina cribrosa and peripapillary scleral position and thickness. *Invest Ophthalmol Vis Sci.* 2007;48:4597–4607.
33. Downs JC, Suh JK, Thomas KA, Bellezza AJ, Burgoyne CF, Hart RT. Viscoelastic characterization of peripapillary sclera: material properties by quadrant in rabbit and monkey eyes. *J Biomech Eng.* 2003;125:124–131.
34. Downs JC, Suh JK, Thomas KA, Bellezza AJ, Hart RT, Burgoyne CF. Viscoelastic material properties of the peripapillary sclera in normal and early-glaucoma monkey eyes. *Invest Ophthalmol Vis Sci.* 2005;46:540–546.
35. Girard MJ, Downs JC, Bottlang M, Burgoyne CF, Suh JK. Peripapillary and posterior sclera mechanics. Part II: experimental and inversse finite element characterization. *J Biomech Eng.* 2009;131:051012.
36. Turner CH. On Wolff's law of trabecular architecture. *J Biomech.* 1992;25:1–9.
37. Gibson LJ, Ashby MF. The mechanics of three-dimensional cellular solids. *Proc R Soc Lond.* 1982;A:43–59.
38. Mehta BS, Colombo EA. Mechanical properties of foamed thermoplastics. *J Cellular Plastics.* 1978;12:59–66.
39. Yang G, Kabel J, van Rietbergen B, Odgaard A, Huiskes R, Cowin SC. The anisotropic Hooke's law for cancellous bone and wood. *J Elast.* 1998;53:125–146.
40. Gibson LJ, Ashby MF. *Cellular Solids: Structures and Properties*. 2nd ed: Cambridge, UK: Cambridge University Press;1999:532.
41. Mills N. *Polymer Foams Handbook: Engineering and Biomechanics Applications and Design Guide.* Oxford, UK: Butterworh-Heinmann; 2007.
42. Cowin SC. Mechanics of materials. In: Cowin SC, ed. *Bone Mechanics Handbook*. Boca Raton: CRC Press; 2001:239–244.

43. Cowin SC, Doty SB. *Tissue Mechanics.* New York: Springer; 2007: 682.
44. Battaglioli JL, Kamm RD. Measurements of the compressive properties of scleral tissue. *Invest Ophthalmol Vis Sci.* 1984; 25:59–65.
45. Downs JC, Yang H, Girkin C, et al. Three-dimensional histomorphometry of the normal and early glaucomatous monkey optic nerve head: neural canal and subarachnoid space architecture. *Invest Ophthalmol Vis Sci.* 2007;48:3195–3208.
46. Bellezza AJ, Rintalan CJ, Thompson HW, Downs JC, Hart RT, Burgoyne CF. Anterior scleral canal geometry in pressurised (IOP 10) and non-pressurised (IOP 0) normal monkey eyes. *Br J Ophthalmol.* 2003;87:1284–1290.
47. Bellezza AJ, Rintalan CJ, Thompson HW, Downs JC, Hart RT, Burgoyne CF. Deformation of the lamina cribrosa and anterior scleral canal wall in early experimental glaucoma. *Invest Ophthalmol Vis Sci.* 2003;44:623–637.
48. Albon J, Purslow PP, Karwatowski WS, Easty DL. Age related compliance of the lamina cribrosa in human eyes. *Br J Ophthalmol.* 2000;84:318–323.
49. Girard MJ, Suh JK, Bottlang M, Burgoyne CF, Downs JC. Scleral biomechanics in the aging monkey eye. *Invest Ophthalmol Vis Sci.* Published online June 3, 2009.
50. Bhandari A, Fontana L, Fitzke FW, Hitchings RA. Quantitative analysis of the lamina cribrosa in vivo using a scanning laser opthalmoscope. *Curr Eye Res.* 1997;16:1–8.
51. Fontana L, Bhandari A, Fitzke FW, Hitchings RA. In vivo morphometry of the lamina cribrosa and its relation to visual field loss in glaucoma. *Curr Eye Res.* 1998;17:363–369.
52. Tezel G, Trinkaus K, Wax MB. Alterations in the morphology of lamina cribrosa pores in glaucomatous eyes. *Br J Ophthalmol.* 2004;88:251–256.
53. Brown DJ, Morishige N, Neekhra A, Minckler DS, Jester JV. Application of second harmonic imaging microscopy to assess structural changes in optic nerve head structure ex vivo. *J Biomed Opt.* 2007;12:024029.
54. Agopov M, Lomb L, La Schiazza O, Bille JF. Second harmonic generation imaging of the pig lamina cribrosa using a scanning laser ophthalmoscope-based microscope. *Lasers Med Sci.* 2009; 24(5):787–792.
55. Levy NS, Crapps EE. Displacement of optic nerve head in response to short-term intraocular pressure elevation in human eyes. *Arch Ophthalmol.* 1984;102:782–786.
56. Yan DB, Coloma FM, Metheetrairut A, Trope GE, Heathcote JG, Ethier CR. Deformation of the lamina cribrosa by elevated intraocular pressure. *Br J Ophthalmol.* 1994;78:643–648.
57. Inoue R, Hangai M, Kotera Y, et al. Three-dimensional high-speed optical coherence tomography imaging of lamina cribrosa in glaucoma. *Ophthalmology.* 2009;116(2):214–222.
58. Srinivasan VJ, Adler DC, Chen Y, et al. Ultrahigh-speed optical coherence tomography for three-dimensional and en face imaging of the retina and optic nerve head. *Invest Ophthalmol Vis Sci.* 2008;49:5103–5110.
59. Fortune B, Yang H, Strouthidis NG, et al. The effect of acute intraocular pressure elevation on peripapillary retinal thickness, retinal nerve fiber layer thickness and retardance. *Invest Ophthalmol Vis Sci.* Published online May 6, 2009.
60. Downs JC, Roberts MD, Burgoyne CF, Hart RT. Finite element modeling of the lamina cribrosa microarchitecture in the normal and early glaucoma monkey optic nerve head. ASME Summer Bioengineering Conference. Keystone, CO: American Society of Mechanical Engineers; 2007.
61. Hernandez MR, Luo XX, Igoe F, Neufeld AH. Extracellular matrix of the human lamina cribrosa. *Am J Ophthalmol.* 1987;104:567–576.
62. Quigley HA, Brown A, Dorman-Pease ME. Alterations in elastin of the optic nerve head in human and experimental glaucoma. *Br J Ophthalmol.* 1991;75:552–557.
63. Girard MJ, Downs JC, Burgoyne CF, Suh JK. Experimental surface strain mapping of porcine peripapillary sclera due to elevations of intraocular pressure. *J Biomech Eng.* 2008;130: 041017.
64. Yang H, Downs JC, Bellezza AJ, Thompson H, Burgoyne CF. 3-D histomorphometry of the normal and early glaucomatous monkey optic nerve head: prelaminar neural tissues and cupping. *Invest Ophthalmol Vis Sci.* 2007;48:5068–5084.